arXiv:1603.07594v1 [cond-mat.mes-hall] 24 Mar 2016

Quantum Hall Edge States in Topological Insulator Nanoribbons

A. Pertsova* and C. M. Canali
Department of Physics and Electrical Engineering, Linnæus University, 391 82 Kalmar, Sweden

A. H. MacDonald
Department of Physics, University of Texas at Austin, TX 78712, USA

We present a microscopic theory of the chiral one-dimensional electron gas system localized on the sidewalls of magnetically-doped Bi_2Se_3-family topological insulator nanoribbons in the quantum anomalous Hall effect (QAHE) regime. Our theory is based on a simple continuum model of sidewall states whose parameters are extracted from detailed ribbon and film geometry tight-binding model calculations. In contrast to the familiar case of the quantum Hall effect in semiconductor quantum wells, the number of microscopic chiral channels depends simply and systematically on the ribbon thickness and on the position of the Fermi level within the surface state gap. We use our theory to interpret recent transport experiments that exhibit non-zero longitudinal resistance in samples with accurately quantized Hall conductances.

PACS numbers: 73.20.r, 73.43.-f
Keywords: topological insulator thin films, edge states, quantum anomalous Hall effect

Introduction—The quantum Hall effect [1] is a transport anomaly that occurs when [2] a two-dimensional electron system has a charge gap, *i.e.* a jump in chemical potential, at a density that depends on magnetic field. It is characterized by the absence of longitudinal resistance and quantized Hall resistance. Both properties can be understood in terms of the chiral one-dimensional electron systems [3] (C1DESs) always present at quantum Hall sample edges. Although the rate at which their non-zero equilibrium currents change as chemical potential is varied is fixed by the magnetic field dependence of the gap density, other properties of C1DESs are dependent on microscopic details. In the case of GaAlAs two-dimensional electron gas systems, for example, it has in fact been difficult to achieve a fully satisfactory understanding of chiral edge state properties because of electrostatic imperatives that force edge reconstructions [4] and cause the number of microscopic edge channels to proliferate [5]. Accurate quantization of the Hall conductance then requires [2] only that local equilibrium be established at decoupled edges of the sample.

In this Letter we address the properties of the chiral one-dimensional electron gas system associated with the quantum anomalous Hall effect (QAHE) [6–16] in magnetically doped topological insulator [17, 18] thin films. The appearance of a quantum Hall effect in these systems is a direct consequence of spontaneously broken time-reversal symmetry, which is also manifested by a suite of unusual magnetic [19–24], and optical [25–27] properties. We show that the chiral one-dimensional electron system associated with this quantum Hall effect is localized on the thin film side walls and that, in contrast to the case of GaAs quantum wells, its microscopic properties depend rather simply on film thickness, the size of the surface state gap induced by broken time-reversal symmetry, and also on the facet dependence of surface-state Dirac-cone velocities. Using our theory, we argue that in the absence of disorder thin films with the characteristics of samples in which the QAHE has so far been studied support a C1DES with a single chiral channel. It follows that the presence of a non-zero longitudinal resistance in most experiments [9, 24, 28–32] cannot be attributed, as is common, to the absence of local equilibrium at a multi-channel edge.

Sidewall State Toy Model— A qualitative understanding of C1DES properties can be obtained from the simplest possible 2D sidewall model. (See Refs. 33–42 for related continuum model analysis.) We assume that the sidewall is infinite in extent in the $\hat{y}$ (horizontal) direction, that it has thickness T in the $\hat{z}$ (vertical) direction [See Fig. 1(a)], and that it is described by an anisotropic Dirac Hamiltonian with a mass term: $\hat{H} = i\hbar(-v_{\mathrm{D}z}\sigma_y\partial_z + v_{\mathrm{D}y}\sigma_x\partial_y) + m(z)\sigma_z$. Here $\sigma = \{\sigma_x, \sigma_y, \sigma_z\}$ is a Pauli-matrix vector that acts on spin, $m(z)$ captures the influence of exchange interactions between the top, bottom, and sidewall surface quasiparticles and the $\hat{z}$ direction bulk magnetization, $v_{\mathrm{D}z}$ is the vertical Dirac velocity, and $v_{\mathrm{D}y}$ the horizontal Dirac velocity. The mass is zero on the side wall where the exchange interaction can be absorbed by a gauge change, ($m(z) = 0$ for $-T/2 < z < T/2$) and has a different sign on the top and bottom surfaces; $m(z) = m_0 > 0$ for $z > T/2$ and $m(z) = -m_0 < 0$ for $z < -T/2$, where m_0 is a constant. We can find the eigenvalues and eigenvectors of this model Hamiltonian by matching wavefunctions at the $z = \pm T/2$ boundaries [43].

The Dirac equation solutions include a set of non-chiral

* Now at: Nordita, KTH Royal Institute of Technology and Stockholm University, Roslagstullsbacken 23, SE-106 91 Stockholm, Sweden; anna.pertsova@su.se

eigenfunctions whose role we focus on in this paper, and a chiral eigenfunction with velocity $v_{\rm D} = \sqrt{v_{{\rm D}z} v_{{\rm D}y}}$, energy $E(k) = \hbar v_{\rm D} k$, and a wavefunction that is constant inside the side wall and decays exponentially on the top and bottom surfaces [See Fig. 1(b)]. The non-chiral eigenvalues are conveniently expressed in dimensionless units related to the sidewall's size-quantization energy scale: $\varepsilon = ET/\pi\hbar v_{{\rm D}z}$, $\mu = m_0 T/\pi\hbar v_{{\rm D}z}$ and $\chi = k\sqrt{v_{{\rm D}y}/v_{{\rm D}z}}T/\pi$. Because the non-chiral band energies are even functions of χ, non-chiral states always appear in equal-energy, opposite-velocity, opposite-wavevector pairs. The number $N_{\rm NC}$ of non-chiral one-dimensional subbands that are occupied at energy ε decreases with dimensionless mass μ, as illustrated in Fig. 1(c) where the energies of non-chiral band minima, located at $\chi = 0$, are plotted as a function of μ. The wavefunctions of the non-chiral states have nodes along the z-direction, with the number of nodes increasing with the energy of the state [Fig. 1(d)]. For thick films, the number of sidewall channels at energies inside the surface-state gap is $N_{\rm NC} \sim \mu = m_0 T/\pi\hbar v_{{\rm D}z} \sim (m_0[\text{meV}]\,T[\text{nm}])/(200\, v_{{\rm D}z}[10^5\text{m/s}])$. It follows that for $\mu \lesssim 1$, non-chiral states are absent across most of the surface state gap. Non-chiral channels are present across a larger fraction of the gap for thicker films, larger gaps, and smaller vertical Dirac velocities. Below we confirm these predictions of the simplified toy model, and obtain a numerical estimate for $v_{{\rm D}z}$ by performing microscopic tight-binding-model calculations.

Microscopic Sidewall State Theory— In order to address transport in the QAHE regime, it is necessary to study the sidewall electronic structure microscopically [10, 34]. This will allow us: i) to determine the velocity parameter $v_{{\rm D}z}$ that along with the film thickness sets the sidewall finite-size quantization energy scale; ii) to examine the position of the Dirac point relative to the bulk conduction and valence bands, and iii) to identify and shed light on relevant features (addressed below) that are not captured by simple continuum models. We focus on Bi_2Se_3 family [44] topological insulators. Electron states in this crystal can be described by a sp^3 tight-binding model with parameters obtained by fitting to *ab initio* calculations [45, 46]. In order to model homogeneous perpendicular magnetization, we introduce an exchange field $B_{\rm ex}$ expressed in energy units and oriented perpendicular to the (111) surface. We comment below on the relationship between $B_{\rm ex}$ and the mass parameter m_0 of the sidewall state toy model.

To extract the facet-dependent surface state Dirac velocities we first consider the infinite cross-sectional-area thin-film geometry. For the Se (111) surface-layer facet, we find that the Dirac cone is isotropic with velocity $v_{\rm D}^0 \approx 5.0 \times 10^5$ m/s. For the $(\bar{1}10)$ sidewall facet, we find that the Dirac cone is strongly anisotropic with $v_{{\rm D}y} \approx 4.8 \times 10^5$ m/s and $v_{{\rm D}z} \approx 2.3 \times 10^5$ m/s. We then turn to the ribbon geometry [Fig. 2(a)] in order to identify the side-wall states active in quantum Hall transport

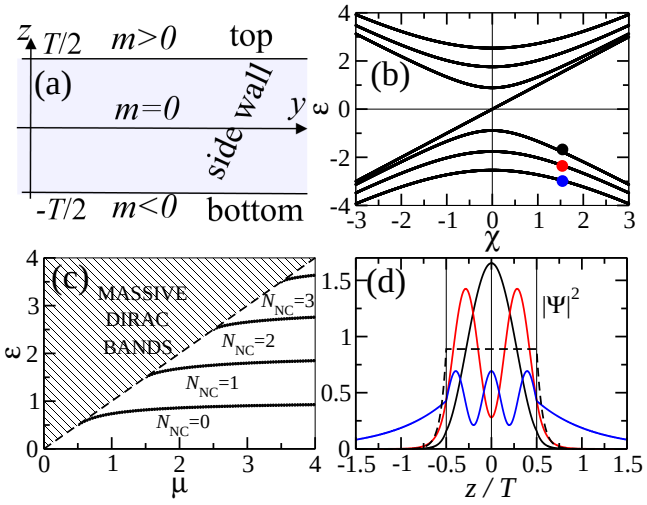

FIG. 1. (Color online) (a) Schematic illustration of a simplified Dirac model for states localized on a y-z plane sidewall. The mass term $m(z)$ in the Dirac Hamiltonian has opposite signs for top ($z > T/2$) and bottom ($z < -T/2$) surfaces and vanishes on the sidewall surface ($-T/2 < z < T/2$). (b) Quasi one-dimensional energy bands calculated at $\mu = 8/\pi$ with energies in $\hbar\pi v_{{\rm D}z}/T$ units. (c) Positive non-chiral band energies at $\chi = 0$ as a function of the dimensionless gap μ. The non-chiral bands are particle-hole symmetric. For $\epsilon > \mu$ all states are extended across the top and bottom surfaces. In the limit $\mu \to \infty$ the dimensionless non-chiral sidewall state energies approach integers. For $\epsilon < \mu$, the $\chi = 0$ band energy lines separate regions labelled by the number of non-chiral channels $N_{\rm NC}$ that are present. (d) Wavefunctions of the chiral state (black dashed line) and the first three negative energy non-chiral states at positive (dimensionless) momentum $\chi = 5/\pi$. The eigenvalues associated with the non-chiral wavefunctions are marked by correspondingly colored dots in (b).

experiments. The ribbon is infinite in the y-direction, the direction of longitudinal transport, has a thickness T in the z-direction approximately equal to 1 nm per quintile layer (QL), and a finite width W in the x-direction. The mixed Bi/Se sidewall $(\bar{1}10)$ surfaces are illustrated in Fig. 2(b), and the Se (111) top and bottom surfaces in Fig. 2(c) [47]. Results for ribbons with $T = 5$QL and $W = 208$nm are presented in Fig. 3.

At $B_{\rm ex} = 0$ the low-energy states consist of discrete quasi-1D channels that are separated in energy by $\sim \hbar\pi v_{\rm D}/(T + W)$ [37] as illustrated in Fig. 3(a). Wavefunctions at energies within the bulk gap, roughly between 0 and 0.4 eV for a 5QL film, are distributed over all four facets of the ribbon at $k = 0$, but because of the Dirac velocity mismatch tend to localize either on sidewall or on surface facets at $k \neq 0$. At exchange field $B_{\rm ex} = 0.16$eV a gap opens and is bridged by a pair of chiral edge states [Fig. 3(b)]. The size of the gap is smaller than the exchange coupling energy because, in contrast to the toy model, the quasiparticles have mixed spin character even at $k = 0$ and g-factors that are smaller than

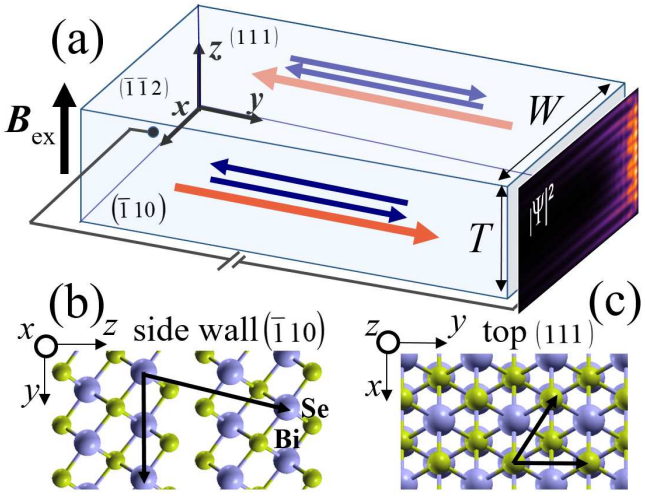

FIG. 2. (Color online) (a) Schematic of a Bi_2Se_3 nanoribbon with finite thickness T and width W. The thick red arrows represent currents carried by ballistic chiral edge states, while the thin blue arrows represent currents carried by ballistic non-chiral edge state channels. The sidewall localization property of chiral states is reflected by the illustrated $|\Psi|^2$ probability density distribution across the ribbon cross section. Top views of the $(\bar{1}10)$ sidewall (b) and the (111) top and bottom surface layers (c), with black arrows for 2D crystal unit vectors.

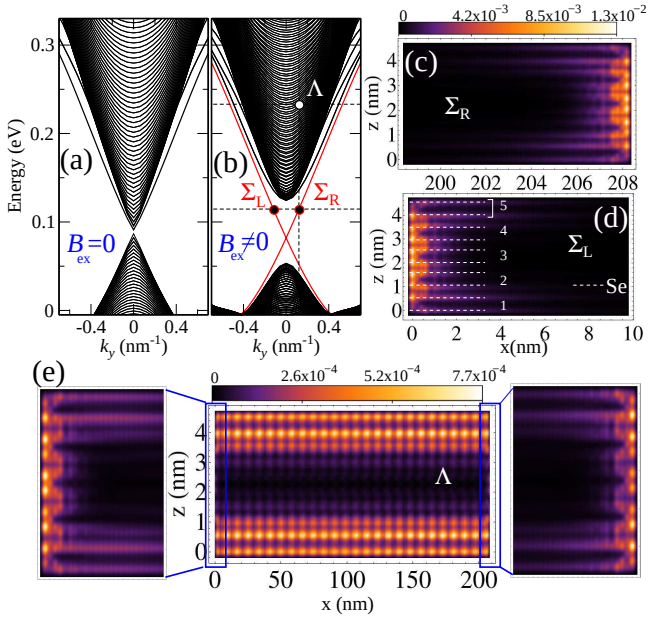

FIG. 3. (Color online) Bandstructure of a Bi_2Se_3 nanoribbon with $T = 5$QL and $W = 208$ nm for $B_{ex} = 0$ (a) and $B_{ex} = 0.16$ eV (b). Chiral edge states are shown in red in panel (b). Spatial distribution of the wavefunction across the ribbon cross-section for a right-goer state Σ_R (c) and a left-goer state Σ_L (d) with energy ≈ 0.11 eV [dashed line in (b)], and a non-chiral state Λ (e) with energy ≈ 0.23 eV [white circle in (b)]. The dashed lines in (d) mark the positions of the outermost Se layers in each QL. In (c) and (d) only the ribbon edges are shown. For this ribbon geometry there are no non-chiral channels that are inside the surface state gap and localized on the sidewalls.

2. The gap in Fig. 3(b) is $\sim 0.07eV$ and can be identified with the gap $2m_0$ in the surface state toy model. It follows that $B_{ex} = 0.16$eV corresponds to $m_0 \sim 35$meV, in agreement with typical experimental estimates. At a given energy, the negative-velocity (Σ_L) and positive-velocity (Σ_R) states (inside the surface state gap) are localized on the opposite side walls [see Fig. 3(c) and (d)]. The value of the chiral-state velocity extracted from the microscopic calculation is $\approx 4.1 \times 10^5$ m/s, which is consistent with the estimate provided by the toy-model expression $v_D = \sqrt{v_{Dz} v_{Dy}} \approx 3.3 \times 10^5$ m/s (evaluated for v_{Dz} and v_{Dy} quoted above). Both states are spin-polarized in the direction of the exchange field.

The chiral edge state wavefunctions are evenly distributed across the sidewalls apart from variations that mirror the chemical structure of the QLs and place larger weight on the Se layers. Chiral states are more strongly localized on the sidewalls at larger k. Non-chiral channels appear in this calculation only at energies outside of the surface state gap. A typical non-chiral state, illustrated in Fig. 3(e) (Λ), has weight on both sidewalls and on the top and bottom surfaces.

The absence of side-wall localized non-chiral transport channels in these calculations can be understood by comparing with the side-wall toy model introduced in the previous section and using the microscopically calculated value for v_{Dz} to evaluate the dimensionless gap parameter. We find that for the thickness and exchange interaction strength of this representative microscopic calculation $\mu \sim 0.3$, consistent with the $N_{NC} = 0$ electronic structure of Fig. 3.(b) Non-chiral channels appear at energies inside the surface state gap only for thicker films or stronger exchange splitting.

Quantum Hall Transition in Very Thin Films— Our sidewall toy model does not account for the hybridization between top and bottom surfaces which, in very thin films, can control a transition between quantum Hall and topologically trivial states. [8] The hybridization scale is negligible compared to typical exchange energy scales in the 5QL films discussed above, but not in the 3QL films whose properties are summarized in Fig. 4. Hybridization plays an essential role in 3QL films by opening a sizable surface state gap at $B_{ex} = 0$. This time-reversed ground state of the 3QL film is a two-dimensional topological insulator and supports helical edge states. The gap decreases in size with increasing B_{ex} and vanishes at $B_{ex} = B_{ex}^{cr}$. For $B_{ex} > B_{ex}^{cr}$ the order of the lowest two-dimensional subbands is reversed, causing a transition to the QAHE phase [43], and the gap size then increases with B_{ex}. We find that $B_{ex}^{cr} \approx 0.09$ eV for 3QL films and that $B_{ex}^{cr} \approx 10^{-2}$ meV for 5QL films. Although remnants of the $B_{ex} = 0$ helical edge states can complicate

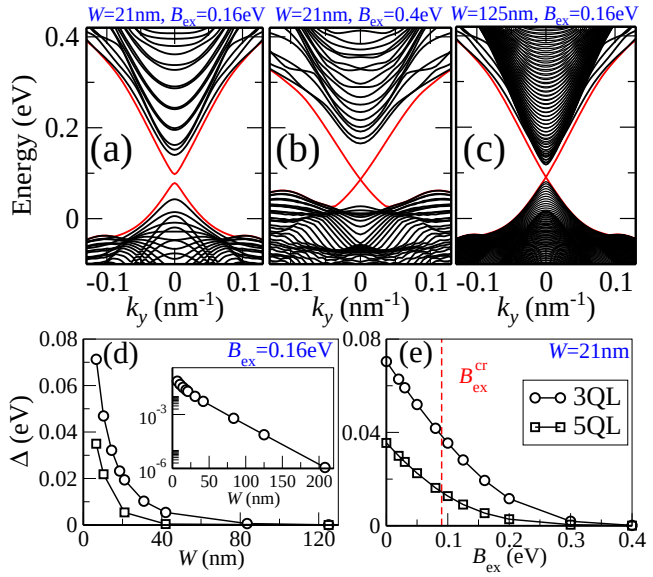

FIG. 4. (Color online) Electronic structure of a Bi_2Se_3 nanoribbon with $T = 3$QL for $W = 21$ nm and $B_{ex} = 0.16$ eV (a), $W = 21$ nm and $B_{ex} = 0.4$ eV (b), and $W = 125$ nm and $B_{ex} = 0.16$ eV (c). Chiral edge states are shown in red. (d) Chiral state avoided crossing gap for $T = 3$QL (circles) and $T = 5$QL (squares) as a function of W for B_{ex}=0.16 eV. The inset shows the logarithm of the gap for 3QL films over a larger range of W's. (e) Energy gap as a function of B_{ex} for a fixed $W = 21$ nm in the same two cases. The vertical dashed line marks the critical exchange field ($B_{ex}^{cr} \approx 0.09$ eV) for 3QL.

edge electronic structure when $B_{ex} \lesssim B_{ex}^{cr}$, our microscopic calculations demonstrate that no trace is present for $B_{ex} \gg B_{ex}^{cr}$ where only the chiral edge modes survive.

For finite width (W) ribbons there is a finite gap in the electronic structure for $B_{ex} > B_{ex}^{cr}$ because of the avoided crossing between edge states localized on opposite side walls. The ribbon gap decreases in size both with increasing B_{ex} [Fig. 4(b)] and increasing W [Fig. 4(c)]. For a fixed exchange field $B_{ex} > B_{ex}^{cr}$ the energy gap decreases exponentially with W [Fig. 4(d)], whereas for $B_{ex} < B_{ex}^{cr}$, the gap approaches a finite value as $W \to \infty$. By fitting the W dependence of the gap to an exponential decay law we estimate that the localization length of the chiral edge state at $B_{ex} = 0.16eV$ is $\lambda \approx 18.6$ nm for 3QLs and $\lambda \approx 8.2$ nm for 5QLs. Since typical experimental samples used in quantum anomalous Hall studies have widths of hundreds of μm, direct coupling between opposite edges is negligible in the absence of disorder.

Quantum Anomalous Hall Effect— Experimental QAHE measurements have so far been performed mainly on films with thicknesses in the range between 5 and 10 QL. Because the vertical sidewall Dirac velocity, which characterizes a direction in which electrons hop between Bi and chalcogen layers, is only a few times smaller than Dirac velocities in directions along Bi layers, we conclude that the 10 QL layer maximum thickness is not sufficient to support non-chiral edge modes. At the same time, hybridization between top and bottom surfaces at the minimum 5QL thickness is very much weaker than typical exchange fields. For this reason, we conclude that the sidewalls of the samples that are typically studied do not support either helical edge states that are a remnant of $B_{ex} = 0$ two-dimensional topological insulator states, or the non-chiral side wall states [10] that are expected in thicker films. The case in which the surface state Dirac point is buried inside the valence band of the host topological insulator might provide an exception to these conclusions, but is not in any case expected to be ideal for the realization of the QAHE.

Because the sidewall spectrum of the QAHE samples consists of a single chiral channel, it is not possible to explain the commonly observed finite longitudinal resistances by assuming a failure to establish local equilibrium on a multi-channel edge. A more likely explanation, in our view, is that potential disorder causes the local Fermi level to sweep across the surface state gap. The relatively high-velocity one-dimensional chiral sidewall states have negligible density of states. Therefore they can do little on their own to screen inevitable spatial variations in external electric fields that induce relative shifts in the Dirac cones of top and bottom surfaces, or external potentials that induce common shifts in the Dirac cones of the two surfaces. Fluctuations that bring the surface states to the Fermi level, provide a mechanism for two-dimensional dissipative transport in some parts of the system. Because the surface states themselves have a large [48, 49], but unquantized Hall conductivity in addition to a finite longitudinal conductivity, surface conduction will tend to lead more to a finite longitudinal conductivity than to a correction to the Hall conductivity.

The quantum Hall effect may be more robust against disorder in thicker films, if they can be grown while maintaining similar sample quality. Because the edge carries current in equilibrium, the presence of many non-chiral channels does not lead either to inaccuracies in Hall quantization or to longitudinal resistance. Instead a larger number of channels at the edge increases the degree to which disorder is screened and helps broaden the gate voltage range over which nearly pure side wall transport can be established.

This work was supported by the Faculty of Technology at Linnaeus University and by the Swedish Research Council under Grant Number: 621-2014-4785. AHM was supported by the Welch Foundation under grant F-1473 and by SHINES, an Energy Frontier Research Center funded by the U.S. Department of Energy (DoE), Office of Science, Basic Energy Science (BES) under award DE-SC0012670. AHM acknowledges valuable interactions with Yabin Fan, Massoud Masir, Pramay Upadhyaya, Kang Wang, Fengcheng Wu and Fei Xue. Computational resources have been provided by the Lunarc center for

scientific and technical computing at Lund University.

[1] K. v. Klitzing, G. Dorda, and M. Pepper, Phys. Rev. Lett. **45**, 494 (1980).
[2] A. H. MacDonald, Mesoscopic Quantum Physics **61**, 659 (1995).
[3] X. Wen, Phys. Rev. B **43**, 11025 (1991).
[4] C. d. C. Chamon and X. G. Wen, Phys. Rev. B **49**, 8227 (1994).
[5] D. B. Chklovskii, B. I. Shklovskii, and L. I. Glazman, Phys. Rev. B **46**, 4026 (1992).
[6] F. D. M. Haldane, Phys. Rev. Lett. **61**, 2015 (1988).
[7] C.-X. Liu, X.-L. Qi, X. Dai, Z. Fang, and S.-C. Zhang, Phys. Rev. Lett. **101**, 146802 (2008).
[8] R. Yu, W. Zhang, H.-J. Zhang, S.-C. Zhang, X. Dai, and Z. Fang, Science **329**, 61 (2010).
[9] C.-Z. Chang, J. Zhang, X. Feng, J. Shen, Z. Zhang, M. Guo, K. Li, Y. Ou, P. Wei, L.-L. Wang, Z.-Q. Ji, Y. Feng, S. Ji, X. Chen, J. Jia, X. Dai, Z. Fang, S.-C. Zhang, K. He, Y. Wang, L. Lu, X.-C. Ma, and Q.-K. Xue, Science **340**, 167 (2013).
[10] J. Wang, B. Lian, H. Zhang, and S.-C. Zhang, Phys. Rev. Lett. **111**, 086803 (2013).
[11] X.-L. Qi, Y.-S. Wu, and S.-C. Zhang, Phys. Rev. B **74**, 085308 (2006).
[12] X.-L. Qi, T. L. Hughes, and S.-C. Zhang, Phys. Rev. B **78**, 195424 (2008).
[13] K. Nomura and N. Nagaosa, Phys. Rev. Lett. **106**, 166802 (2011).
[14] K. He, Y. Wang, and Q.-K. Xue, National Science Review (2013), 10.1093/nsr/nwt029.
[15] X. Kou, Y. Fan, M. Lang, P. Upadhyaya, and K. L. Wang, Solid State Communications **215216**, 34 (2015).
[16] H. Weng, R. Yu, X. Hu, X. Dai, and Z. Fang, Advances in Physics **64**, 227 (2015).
[17] M. Z. Hasan and C. L. Kane, Rev. Mod. Phys. **82**, 3045 (2010).
[18] X.-L. Qi and S.-C. Zhang, Rev. Mod. Phys. **83**, 1057 (2011).
[19] Y. Tserkovnyak and D. Loss, Phys. Rev. Lett. **108**, 187201 (2012).
[20] J.-J. Zhu, D.-X. Yao, S.-C. Zhang, and K. Chang, Phys. Rev. Lett. **106**, 097201 (2011).
[21] Y. L. Chen, J.-H. Chu, J. G. Analytis, Z. K. Liu, K. Igarashi, H.-H. Kuo, X. L. Qi, S. K. Mo, R. G. Moore, D. H. Lu, M. Hashimoto, T. Sasagawa, S. C. Zhang, I. R. Fisher, Z. Hussain, and Z. X. Shen, Science **329**, 659 (2010).
[22] J. G. Checkelsky, J. Ye, Y. Onose, and Y. Tokura, Nature Physics **8**, 729 (2012).
[23] S.-Y. Xu, M. Neupane, C. Liu, D. Zhang, A. Richardella, L. A. Wray, N. Alidoust, M. Leandersson, T. Balasubramanian, J. Sánchez-Barriga, O. Rader, G. Landolt, B. Slomski, J. H. Dil, J. Osterwalder, T.-R. Chang, H.-T. Jeng, H. Lin, A. Bansil, N. Samarth, and M. Z. Hasan, Nature Physics **8**, 616 (2012).
[24] S. Grauer, S. Schreyeck, M. Winnerlein, K. Brunner, C. Gould, and L. W. Molenkamp, Phys. Rev. B **92**, 201304 (2015).
[25] W.-K. Tse and A. H. MacDonald, Phys. Rev. Lett. **105**, 057401 (2010).
[26] A. G. Mal'shukov, H. Skarsvåg, and A. Brataas, Phys. Rev. B **88**, 245122 (2013).
[27] M. Lasia and L. Brey, Phys. Rev. B **90**, 075417 (2014).
[28] J. Checkelsky, R. Yoshimi, A. Tsukazaki, K. S. Takahashi, Y. Kozuka, J. Falson, M. Kawasaki, and Y. Tokura, Nature Physics **10**, 731 (2014).
[29] X. Kou, S.-T. Guo, Y. Fan, L. Pan, M. Lang, Y. Jiang, Q. Shao, T. Nie, K. Murata, J. Tang, Y. Wang, L. He, T.-K. Lee, W.-L. Lee, and K. L. Wang, Phys. Rev. Lett. **113**, 137201 (2014).
[30] A. J. Bestwick, E. J. Fox, X. Kou, L. Pan, K. L. Wang, and D. Goldhaber-Gordon, Phys. Rev. Lett. **114**, 187201 (2015).
[31] C.-Z. Chang, W. Zhao, D. Y. Kim, H. Zhang, B. A. Assaf, D. Heiman, S.-C. Zhang, C. Liu, M. H. W. Chan, and J. S. Moodera, Nature Physics **14**, 473 (2015).
[32] C.-Z. Chang, W. Zhao, D. Y. Kim, P. Wei, J. K. Jain, C. Liu, M. H. W. Chan, and J. S. Moodera, Phys. Rev. Lett. **115**, 057206 (2015).
[33] W.-K. Lou, F. Cheng, and J. Li, Journal of Applied Physics **110**, 093714 (2011).
[34] F. W. Chen, L. A. Jauregui, Y. Tan, M. Manfra, G. Klimeck, Y. P. Chen, and T. Kubis, Applied Physics Letters **107**, 121605 (2015).
[35] O. Deb, A. Soori, and D. Sen, Journal of Physics: Condensed Matter **26**, 315009 (2014).
[36] Y.-Y. Zhang, X.-R. Wang, and X. C. Xie, Journal of Physics: Condensed Matter **24**, 015004 (2012).
[37] J. H. Bardarson, P. W. Brouwer, and J. E. Moore, Phys. Rev. Lett. **105**, 156803 (2010).
[38] G. Rosenberg, H.-M. Guo, and M. Franz, Phys. Rev. B **82**, 041104 (2010).
[39] Y. Zhang and A. Vishwanath, Phys. Rev. Lett. **105**, 206601 (2010).
[40] K. Chang and W.-K. Lou, Phys. Rev. Lett. **106**, 206802 (2011).
[41] L. Brey and H. A. Fertig, Phys. Rev. B **89**, 085305 (2014).
[42] S. Acero, L. Brey, W. J. Herrera, and A. L. Yeyati, Phys. Rev. B **92**, 235445 (2015).
[43] See Supplemental Material at ... for a detailed description of the toy model for the side-wall states and for a discussion of the exchange-field driven transition from a trivial to a quantum anomalous Hall insulator in topological-insulator thin films.
[44] D. Hsieh, Y. Xia, D. Qian, L. Wray, J. H. Dil, F. Meier, J. Osterwalder, L. Patthey, J. G. Checkelsky, N. P. Ong, A. V. Fedorov, H. Lin, A. Bansil, D. Grauer, Y. S. Hor, R. J. Cava, and M. Z. Hasan, Nature **460**, 1101 (2009).
[45] K. Kobayashi, Phys. Rev. B **84**, 205424 (2011).
[46] A. Pertsova and C. M. Canali, New Journal of Physics **16**, 063022 (2014).
[47] Y.-L. Lee, H. C. Park, J. Ihm, and Y.-W. Son, Proceedings of the National Academy of Sciences **112**, 11514 (2015).
[48] N. A. Sinitsyn, A. H. MacDonald, T. Jungwirth, V. K. Dugaev, and J. Sinova, Phys. Rev. B **75**, 045315 (2007).
[49] N. A. Sinitsyn, Journal of Physics: Condensed Matter **20**, 023201 (20